Optics & Laser Technology 203 (2026) 115538

Contents lists available at ScienceDirect

Optics and Laser Technology

journal homepage: www.elsevier.com/locate/jolt

Full length article

Rapid quantitative characterization of ultrasonic fields using Fizeau interferometry

Regina Schuster [a,*], Marius Foith [a], Jan Helge Dörsam [b], Sören Soennecken [b], Yannick Schrödel [c,d,e], Christoph M. Heyl [c,d,e], Mario Kupnik [b], Anne Harth [a]

[a] Center for Optical Technologies, Aalen School of Applied Photonics, Aalen University of Applied Sciences, Aalen, Germany
[b] Measurement and Sensor Technology Group, Technische Universität Darmstadt, Darmstadt, Germany
[c] Deutsches Elektronen-Synchrotron DESY, Hamburg, Germany
[d] Helmholtz Institute Jena, Jena, Germany
[e] GSI Helmholtzzentrum für Schwerionenforschung GmbH, Darmstadt, Germany

HIGHLIGHTS

- A contactless method for characterizing high-power ultrasonic fields is required.
- Fizeau interferometry is applied for rapid quantitative 2D characterization.
- Sound-induced refractive index modulations are measured interferometrically.
- Fizeau interferometric sound field visualizations are compared with Schlieren images.
- Quantitative interferometric results are validated using an optical microphone.

ARTICLE INFO

Keywords:
Interferometry
Fizeau interferometer
Optical path differences
Refractive index modulation
Ultrasonic waves
Air-coupled ultrasound characterization

ABSTRACT

The accurate characterization of air-coupled high-power (sound pressure level SPL_{min} > 120 dB) ultrasonic fields is essential for advancing the development and control of ultrasonic transducer arrays. Conventional characterization methods often fail to provide both contactless visualization and a quantitative sound pressure distribution without the need for time-consuming point-by-point scanning. Acoustic pressure variations modulate the refractive index of the medium, e.g., ambient air, and thereby change the optical path length, which can be measured interferometrically. In this paper, Fizeau interferometry is systematically compared with Schlieren imaging and optical microphone measurements. The results show strong agreement with these reference methods and confirm the reliability of the interferometric approach. The key contribution of this study is the demonstration that Fizeau interferometry enables simultaneous contactless two-dimensional field visualization and rapid, quantitative sound pressure mapping. In contrast to conventional methods, the proposed approach combines a full-field ($Ø_{sample}$ = 2″) acquisition within 40 ms without scanning at a high spatial resolution of 23 µm and quantitative capability. Consequently, it provides a rapid tool for characterizing ultrasonic fields in applications such as acoustic levitation or sono-photonic systems.

1. Introduction

Air-coupled ultrasonic fields play a fundamental role in numerous applications, ranging from industrial use cases such as contactless material testing [1,2] and acoustic levitation [3–5] to medical technology [2,6]. Developments have demonstrated that intense ultrasonic fields can even be used to control, modulate, and deflect high-power optical beams [7]. To understand, control, and optimize these often complex and non-stationary ultrasonic fields, effective characterization methods are required.

Traditional, non-optical approaches using acoustic microphones are physically limited in spatial resolution [8] due to their aperture sizes (ca. 1 mm to 10 mm [9,10]). This indicates that, particularly for ultrasonic frequencies (f_{sound} > 20 kHz), achieving sufficient spatial resolution for sound field characterization is impractical. However,

* Corresponding author.
Email address: regina.schuster@hs-aalen.de (R. Schuster).

https://doi.org/10.1016/j.optlastec.2026.115538
Received 26 February 2026; Received in revised form 17 April 2026; Accepted 12 May 2026
Available online 20 May 2026

alternative approaches for smaller ultrasonic microphones exist, such as the miniature ferroelectret microphone [11]. It is characterized by a broadband ultrasonic frequency range, high sensitivity, and a diameter of 0.5 mm. Standard microphones are additionally restricted in their upper limit of sound pressure level SPL (see Eq. (7)) with a typical acoustic overload point of $SPL_{max} = 130$ dB [12]. This is often not high enough for characterizing acoustic levitators or high-power ultrasonic fields ($SPL_{required} \approx 150$ dB). Even when using special high-level microphones [13], the transducers to be measured are typically operated at a reduced voltage to avoid saturation and nonlinearities of the microphone [14]. This configuration often does not correspond to the actual application to be investigated. As microphones are placed directly within the sound field, disturbing feedback effects, scattering, or absorption will occur. One of the most significant challenges of microphone-based techniques is the restriction to measure only a single point, necessitating a scanning process to reconstruct the sound field. Consequently, point-by-point acoustic microphone scans are not only time-consuming; they are often scientifically inadequate. Moreover, in certain setups, such as modern transducer array geometries [15] or specific high-pressure environmental conditions [16], even an ideal microphone becomes practically unusable due to its design, accessibility, or field geometry.

Another technique is using optical microphones, e.g., from Xarion [17]. They measure the pointwise sound pressure level based on refractive index changes using a Fabry-Pérot interferometer. Here, a scanning process can be used to obtain an approximate 2D slice from a 3D sound field (x, y, z).

In general, optical methods have gained attention due to their potential to provide high-resolution imaging without direct interaction with the sound field. A well-known method to map ultrasonic fields is laser Doppler vibrometry [18,19]. In this approach, the laser beam propagates through the acoustic field and is subsequently reflected by a stationary mirror rather than a vibrating surface. This configuration enables the projection of the three-dimensional acoustic field onto a two-dimensional (x, y) plane, thereby obtaining the quantitative sound pressure.

The laser Doppler vibrometry, along with other conventional or optical microphones, faces a significant limitation: The pointwise measurement techniques require sequential scanning of the field, which is time-consuming. In practice, this poses a significant downside, as the field distribution of non-stationary air-coupled ultrasound can change over time due to various factors. The reasons include heating of the transducer, acoustic streaming, drift, detuning, and environmental changes. Real-time data is imperative for measuring the transient development of a resulting sound field, particularly when working with transducer arrays or acoustic levitators. For this reason, there is a need for alternatives, such as reducing the number of measurements and reconstructing the sound field [19] or using a non-scanning full-field implementation [20].

However, Schlieren imaging enables real-time and 2D visualization of ultrasonic fields in a non-contact way [21]. This is a simple method to visualize a two-dimensional projection image of sound-induced refractive index gradients, although in general, it does not directly provide quantitative data. Another method, the thermal camera-based characterization of ultrasonic fields, also allows direct 2D imaging and even quantitative sound pressure measurements, but it requires placing a mesh in the sound field, which leads to a not entirely contactless technique [22].

This gap motivates research into a contactless technique that enables high-resolution, two-dimensional, rapid imaging (ideally single-shot) for realistic ultrasonic “high-power” applications in combination with quantitative sound pressure data.

Note: The definition of “high-power” in the context of this study is $SPL_{min} > 120$ dB and it is not exclusively associated with nonlinear acoustic phenomena. The primary scope of this work is the characterization of acoustic fields at elevated pressure levels, while remaining within the regime where linear acoustic approximations are valid (on the order of $SPL_{max} \lesssim 155$ dB). However, at particularly high sound pressure levels, acoustic nonlinearities are to be expected. A compact introduction to nonlinear acoustic effects and their impact on the proposed measurement method can be found in Appendix A.

In this paper, an interferometer is investigated, the so-called Fizeau interferometer, which is usually used to determine the surface roughness of high-end glass workpieces after robot polishing [23]. The setup generates a 2D projection image of the optical path difference depending on the surface of the workpiece. Since the ultrasonic pressure modulation also changes the refractive index of air, the data obtained are proportional to the integral of the sound pressure along the propagation direction of the laser. By pulsing this laser synchronized to the ultrasonic frequency, with a controllable time delay, the interferometer can be used to measure temporally oscillating sound pressure modulations. The significant difference in propagation velocity between light and sound waves ($c_{light} \gg c_{sound}$) in air enables the acquisition of basically any oscillation state of the acoustic wave. With this modification, the Fizeau interferometer is employed for **contactless 2D visualization** at a **high spatial resolution**, and **rapid quantitative characterization** of air-coupled high-power ultrasonic waves.

This study demonstrates the capabilities of a Fizeau interferometer (Section 2.2) and successfully validates its performance by comparing the results against two established methods. These techniques represent the current state-of-the-art for qualitative and quantitative analysis, respectively: Schlieren imaging (Section 3.1) and Xarion microphone measurements (Section 3.2).

2. Methodology

2.1. Ultrasonic source

The acoustic field for all experiments was generated using an ultrasonic phased array [24] consisting of 8×8 transducers (MA40S4S, Murata, Kyoto, Japan) and controlled by an FPGA (Zynq 7000 SoC, AMD, San José, USA). The transducers are driven by an ultrasound pulser chip (HV7355, Microchip Technology Inc., Arizona, USA), providing a rectangular signal with a frequency of 40 kHz and a peak-to-peak voltage of 20 V. The emitted sound waves are concentrated into a smaller acoustic aperture by a 3D-printed waveguide structure with a total output aperture width of $w_{aperture} = 33$ mm (cf. Fig. 1). In the following, this system, including the array of ultrasonic transducers and the waveguide structure, is called the *transducer array*. The transducer array operates at a sound frequency of $f_{sound} = 40$ kHz and achieves a sound pressure level of SPL = 145 dB measured with a microphone in the main lobe at a distance of 0.3 m, if all transducers are in phase [25].

The ambient temperature during the experiments was 20.6 °C, resulting in a speed of sound $c_{sound} = 343.7$ m/s and a corresponding acoustic wavelength $\lambda_{sound} = \frac{c_{sound}}{f_{sound}} = 8.6$ mm.

The time-dependent sound wave, propagating in the x direction can be described by its pressure amplitude p_0 as follows [26]:

$$p_{prop}(x,t) = p_0 \cdot \cos\left[\left(\frac{2\pi}{\lambda_{sound}} \cdot x\right) - \left(2\pi f_{sound} \cdot t\right)\right]. \quad (1)$$

The corresponding coordinate system is indicated in Fig. 1. In order to increase the sound pressure, a standing wave is generated by placing an acoustic reflector parallel to the transducer array. With this simple arrangement, it should be possible to achieve an increase in sound pressure by a factor of 2. Therefore, the reflector is positioned at the distance of maximum overall sound pressure, which is at $L \approx q \cdot \frac{\lambda_{sound}}{2}$, where $q = 11$ is an integer [27–30]. The resulting standing sound field $p_{stand}(x,t) \hat{=} p_{sound}(x,t)$ is described, in linear approximation, by [26]:

$$p_{stand}(x,t) = 2p_0 \cdot \cos\left(\frac{2\pi}{\lambda_{sound}} \cdot x\right) \cdot \cos\left(2\pi f_{sound} \cdot t\right). \quad (2)$$

In this configuration, the antinodes of the standing wave oscillate over time t between their minimum and maximum pressure values. It

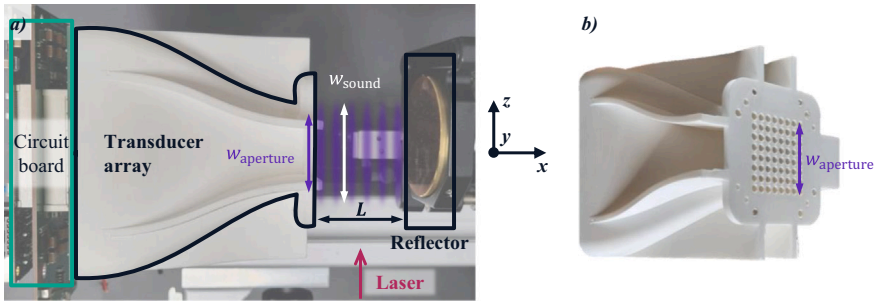

Fig. 1. A) Side view of the ultrasonic system to be measured. The arrangement consists of the transducer array, including a circuit board and a 3D-printed waveguide structure with an acoustic output aperture width $w_{aperture}$. An ultrasonic reflector is positioned at a distance L to generate plane, standing sound waves (indicated by purple shading) with a sound field width w_{sound}. The sound field width w_{sound} can be approximated by the aperture width $w_{aperture}$. The coordinate system indicates the orientation of the arrangement, with sound waves propagating mainly in the x-direction and the laser propagating in the z-direction in the interferometric setup. B) Perspective view of the transducer array with the output aperture width $w_{aperture}$ indicated.

should be noted that the subsequent interferometric method does not require the use of a reflector. Applying the "synchronized mode" (see Section 2.2.1) enables imaging of propagating waves. Additionally, the increase in sound pressure induced by the reflector is not a critical factor regarding the lower sound pressure limit (see Section 4.1) of the Fizeau interferometer. When the sound pressure becomes exceedingly high, thereby inducing nonlinear acoustic effects, such as waveform steepening, the sound waves deviate from their sinusoidal nature. Consequently, the linear approximation (Eq. (2), Eq. (5), and Eq. (6)) becomes inadequate for the quantitative analysis of sound pressure. Nonlinear phenomena are addressed in more detail in Appendix A.

2.2. Fizeau interferometer

The hypothesis is that an ultrasonic field with an SPL = 145 dB (Section 2.1) can be both visualized and quantified using interferometry.

This is confirmed by other techniques that either make acoustic changes visible with an interferometer [31,32] or measure quantitative sound pressure data [33,34]. An interferometer measures an optical path difference (OPD) and in the scope of this paper, the OPD is caused by a modulation of an ultrasonic field in air. When the interferogram is captured with a camera, a two-dimensional $OPD(x, y)$ is obtained, which depends on the refractive index modulation $n_{sound}(x, y)$, the sound field width w_{sound}, the sound-induced phase shift φ and the laser wavelength λ_{laser}:

$$OPD(x, y) = n_{sound}(x, y) \cdot w_{sound} = \frac{\lambda_{laser}}{2\pi} \cdot \varphi(x, y). \tag{3}$$

Here, $n_{sound}(x, y)$ is the change in the refractive index due to sound. The corresponding absolute optical path length is $OPL = \left(n_{sound}(x, y) + n_{air}\right) \cdot w_{sound}$. In the experimental setup, the sound waves propagate in the x direction and the laser beam in the z direction. In practice, it is challenging to measure the width of the sound field w_{sound} along the z direction. Thus, there are several methods to determine the sound field width w_{sound}. Three of them are discussed here. A graphical overview and more details are given in the Appendix B.

I.: In first approach, the sound field width w_{sound} can be approximated as constant [35] using the width of the output aperture $w_{aperture}$ of the waveguide structure. This represents a simple and straightforward approach.

II.: The second method is based on experimental data, making it a more accurate representation of reality. It is built on the assumption, that the sound field is rotationally symmetric by 90° steps. This implies that $n_{sound}(x, y) = n_{sound}(x, z)$ and furthermore, the values for the sound field width are identical: $w_{sound,y}(x) = w_{sound,z}(x)$. The sound field width w_{FWHM} is determined by calculating the full width at half maximum (FWHM) from the interferogram's phase shift data $\varphi(x, y)$. This approach can easily be implemented in the evaluation processing of the interferometric data, but requires that the sample area exceeds the width w_{FWHM} of the sound field.

III.: The third method employs a simulation (angular spectrum approach [36]) and is additionally used for the validation of Method II. The result of the simulation is a pixel-dependent effective sound field width $w_{eff}(x_i, y_j)$. A detailed explanation of the simulation can be found in Appendix B.1.

In general, the sound field width acts as a scaling factor for the quantitative sound pressure level.

From now on, w_{sound} is replaced with the effective sound field width $w_{eff}(x_i, y_j)$, but another kind of width determination could also be applied. Thus, the sound-induced refractive index modulation is obtained:

$$n_{sound}(x, y) = \frac{OPD(x, y)}{w_{eff}(x_i, y_j)}. \tag{4}$$

Note that, in general, the refractive index depends on parameters such as temperature, pressure, etc., described by the modified Edlén equations [37,38]. An approximation is applied in which only influences resulting from deviations from normal pressure ($\frac{\Delta p}{p_{air}}$) and ambient temperature ($\frac{\Delta T}{T_{air}}$), as well as the refractive index of air n_{air} (at T_{air} = 20.6 °C), are considered. In this case, the pressure deviation $\Delta p = p_{sound}$ corresponds to the sound-induced changes:

$$n_{sound} = \left(n_{air} - 1\right) \cdot \left(\frac{\Delta p}{p_{air}} + \frac{\Delta T}{T_{air}}\right). \tag{5}$$

For adiabatic conditions (laser frequency $\nu_{laser} \gg f_{sound}$), the influence of temperature can be neglected [39] and the following linear approximation can be used:

$$p_{sound}(x, y) = \frac{n_{sound}(x, y)}{n_{air} - 1} \cdot p_{air}. \tag{6}$$

This equation assumes that the entire change in refractive index is caused by sound pressure modulations. Thus, measuring two-dimensional interferograms enables the quantitative estimation of the sound pressure at a certain position (x, y).

In order to enable a more straightforward comparison of sound pressure, in Eq. (7) the logarithmic relationship to the sound pressure level is provided. Therefore, using the effective value $p_{sound,rms}(x, y) = \frac{p_{sound}(x,y)}{\sqrt{2}}$ for sinusoidal waves and the hearing threshold as the reference sound pressure of p_{ref} = 20 µPa [26], it follows that:

$$\mathrm{SPL}(x, y) = 20\ \mathrm{dB} \cdot \log_{10}\left(\frac{|p_{sound,rms}(x, y)|}{p_{ref}}\right). \tag{7}$$

2.2.1. Fizeau interferometer setup

For this study, an adapted replica of the Fizeau interferometer *Zeiss DIRECT 100 NT* [40] is used. The main advantage of the Fizeau principle over other interferometric imaging techniques [41] is that it operates as a common path interferometer. The reference and sample beams share nearly identical optical paths, which minimizes sensitivity to environmental noise compared to Michelson or Mach–Zehnder interferometers. Only within the sample area, the beams differ, allowing an optical path difference to be detected with subnanometer precision in air [23,40]. The sample area is defined by the size ($\emptyset_{\text{sample}} = 2'' = 50.8$ mm) and distance ($d_z = 15$ cm) of the reference and the sample plates. The overall quality of the measurements is limited by the properties of the optics used, such as surface flatness. The reference and sample plates (WW12012, Thorlabs, Bergkirchen, Germany) have a surface flatness over the central (Ø15 mm) of $\leq \frac{\lambda_{\text{laser}}}{20}$ and over the entire clear aperture ($\geq$ Ø45.72 mm) of $\leq \frac{\lambda_{\text{laser}}}{10}$ at a wavelength of 633 nm.

The setup (see Fig. 2) employs a helium–neon laser (05 LHP 071-2, Mells Griot, Bonn, Germany) with a wavelength of $\lambda_{\text{laser}} = 632.8$ nm, which is expanded using a lens L1 $\left(f_1' = 10\text{ mm},\ \emptyset_1 = \frac{1}{4}''\right)$ and a collimator L2 ($f_2' = 500$ mm, $\emptyset_2 = 4''$). A motorized diffuser rod (DG20-1500-H2-MD, Thorlabs, Bergkirchen, Germany) destroys the spatial coherence to reduce speckles (not shown). The reference beam is reflected at a wedged reference plate ($R \approx 4\%$), while the sample beam passes twice through the sample area. The ultrasonic field to be investigated modulates the refractive index. This modification changes the wavefront of the sample beam, thereby generating an optical path difference between the reference and sample beams. The resulting interference pattern can be acquired using a camera (U3-3090SE-M-GL Rev.1.2, IDS, Obersulm, Germany). The magnification of the lenses L2 ($f_2' = 500$ mm) and L3 ($f_3' = 75$ mm, LA1608-633, Thorlabs, Bergkirchen, Germany) and the camera's 4096 px×2160 px with a size of $d_{\text{px}} = 3.45$ µm enable a spatial resolution of 23 µm in the sample area. The spatial resolution achieved significantly exceeds that of the Schlieren setup (cf. Section 2.3). This effect mainly, but not exclusively, arises from the better camera properties in the interferometric setup. In this setup, even with identical camera specifications, the spatial resolution of the Fizeau interferometer is expected to be better. Even when compared to other methods, such as the reconstruction of sound fields from laser Doppler vibrometry measurements [19], the spatial resolution of Fizeau interferometry stands out. In general, the use of a laser as a light source in an interferometer benefits from spatial coherence, less chromatic aberration, and higher sensitivity in z direction.

The fringe data evaluation is based on spatial carrier frequency analysis implemented in Python. The carrier frequency is generated by tilting the sample plate with respect to the reference plate. The spatial carrier frequency analysis and the simultaneous phase-shifting method [43] belong to the interferometric single-shot approaches. These techniques have an advantage over temporal phase-shifting interferometry since only a single interferogram is sufficient for reconstruction: A Fourier transform extracts the spectral components, a bandpass filter isolates the carrier, and demodulation provides the phase. Aberrations are suppressed by removing Zernike modes [44] using "High Contrast Imaging for Python" (HCIPy) [45], ensuring independence from imperfections of optical components [23]. In addition, the background is subtracted, and the data are divided by two (because of the double beam passes through the sound field). Using the extracted phase shift $\varphi(x, y)$, quantitative evaluations can be performed, such as determining the sound frequency. Furthermore, with this phase, the optical wavelength λ_{laser}, and the effective width of the sound field $w_{\text{eff}}(x_i, y_j)$, the refractive index modulation is calculated as:

$$n_{\text{sound}}(x, y) = \frac{\lambda_{\text{laser}}}{2\pi \cdot w_{\text{eff}}(x_i, y_j)} \cdot \varphi(x, y). \tag{8}$$

The estimated refractive index modulation due to the ultrasonic field is on the order of magnitude of $n_{\text{sound}} \approx 10^{-6}$. Finally, to obtain the two-dimensional sound pressure distribution $p_{\text{sound}}(x, y)$ from the refractive index, Eq. (6) is applied.

The total processing algorithm of the interferograms requires less than 30 s and has not yet been specifically optimized for computational speed, still remaining significantly faster than conventional scanning-based methods.

A major benefit of the Fizeau interferometer is the scanning-free recording of the entire acoustic field within a single acquisition (40 ms) event of the camera. The rapid data acquisition of the entire sound field is intended to prevent significant temperature-induced changes in the ultrasonic field from occurring during the measurement process. However, due to the temporal oscillation of ultrasound, synchronization is required. Since the camera exposure exceeds the ultrasonic period, the laser (continuous wave) is pulsed with an acousto-optic modulator (632FSAOM-80-1.0, AeroDIODE, Bègles, France) with its driver (RFAOM-T-80, AeroDIODE, Bègles, France) and triggered by the sound frequency of the transducer array ($f_{\text{sound}} = 40$ kHz). A delay tool (24E10 121, AeroDIODE, Bègles, France) adjusts pulse width and phase delay. This procedure ensures that the ultrasonic field is always illuminated at a consistent temporal oscillation state throughout the entire

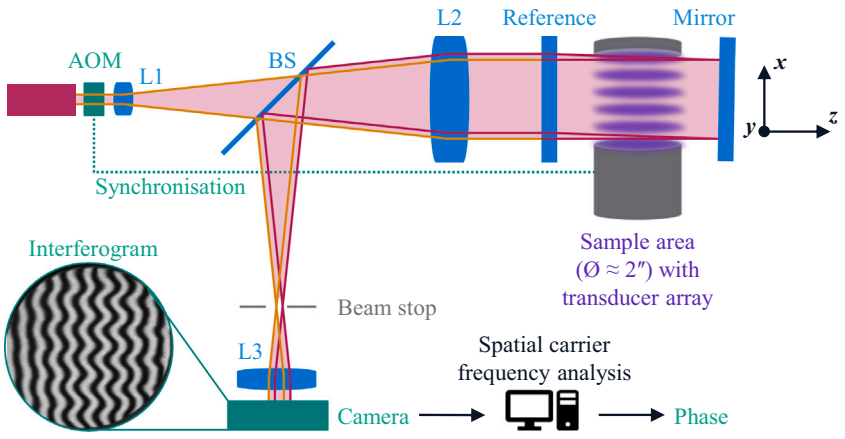

Fig. 2. Schematic representation of the Fizeau interferometer setup to visualize ultrasonic fields. The laser is expanded and collimated with the lenses L1 and L2. Refractive index modulations in the sample area cause modulations of the sample wavefront and thus an optical path difference between the sample beam (red) and the reference beam (orange). The acousto-optic modulator AOM is used to pulse the laser and synchronize it to the ultrasonic frequency. The beam splitter BS (BSW16, Thorlabs, Bergkirchen, Germany) directs the interfering beams through an eyepiece L3 onto a camera. There, the interferogram is captured and then digitally processed to obtain the phase modulation caused by the ultrasonic field. Modified representation based on [42].

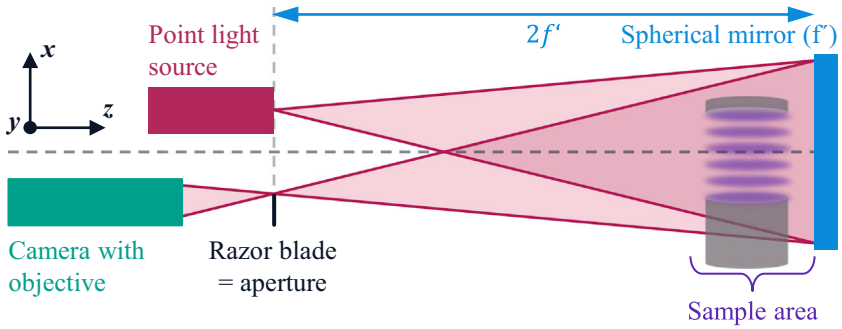

Fig. 3. Schematic representation of the Schlieren setup; the refractive index gradients in the sample area cause light deflection, which leads to brighter and darker regions on the camera due to the aperture (razor blade). Modified representation based on [47].

exposure time of the camera. In this way, the resulting refractive index modulation is prevented from being averaged out due to continuous illumination. This operation mode is referred to as "synchronized mode".

Systematic errors, temperature drifts, or vibrations can be reduced by background subtraction and averaging. As the transducer array heats up during operation, temperature changes are carefully monitored, ensuring stable quantitative measurements [40].

The current setup allows full control of camera parameters, providing flexibility for different applications. This is an improvement over the approach described in [46], where the camera parameters are not directly accessible.

2.3. Schlieren imaging

The Schlieren technique [21] serves as a typical method for contactless visualization of the sound field. Fig. 3 shows the schematic representation of the Schlieren setup. A point light source is focused onto an aperture (a razor blade). Sound waves and the corresponding refractive index gradients in the sample area deflect parts of the light beam, causing them to be either blocked or passed by the aperture. This creates a pattern of bright and dark regions on the camera, effectively generating an image of the gradient of the sound field [21].

The camera (U3-31A0SE-C-HQ Rev.1.2, IDS, Obersulm, Germany) operates with a single acquisition event. This cannot be considered a typical single-shot measurement, since the exposure time exceeds one acoustic period. Nevertheless, only one camera frame ($t_{\text{frame}} = 40$ ms) is captured, allowing for rapid single-frame acquisition despite the temporal averaging of the signal. The light source (pulse-driven LED) is triggered by the ultrasonic frequency to prevent the signal from being integrated over different oscillation states of the sound field. The spatial resolution in the sample area (field of view: 352 mm × 269 mm) with the camera (816 px × 624 px) used is 431 µm.

A disadvantage of the Schlieren method is that gradients in the direction of the aperture edge cannot be detected, and if spatial resolution is an issue, Schlieren imaging is often not the best choice. Moreover, in its conventional implementation, this technique provides only a qualitative impression of the sound field but no quantitative results. However, there are alternative approaches that address this issue [4,48,49]. Nevertheless, these approaches still have some disadvantages. The razor blade in the Schlieren setup works as an aperture and blocks some of the light. This reduces the brightness of the light source, which can lead to complications in cases that are close to the detection limit. The limited electrical modulation bandwidth of the LED makes synchronization between the light source and the sound field difficult for higher ultrasound frequencies.

2.4. Xarion optical microphone

To provide a quantitative measurement for sound pressure measurements, the Xarion optical microphone (Eta 100 Ultra, XARION Laser Acoustics GmbH, Vienna, Austria) [17] is used. Its working principle is based on a Fabry-Pérot interferometer that detects sound-induced modulations of the refractive index of air within its cavity. This optical detection results in an electrical signal proportional to the sound pressure amplitude (rms value). The microphone head has a diameter of 5 mm. Since it is an optical method, it features no moving parts, enabling a wide frequency bandwidth (10 Hz < $f_{\text{bandwidth}}$ < 1 MHz) and a large dynamic range (100 dB), making it a highly sensitive and precise instrument [50].

However, the primary limitation of this method is its localized, point-by-point nature, which necessitates a time-consuming scanning process to characterize a two-dimensional field. In our setup, line scans along the y-axis (at $z = 0$, $x = 0$, which is the center between the transducer array and reflector) were performed manually using a linear stage with a step size of $\Delta y = 2$ mm. The electrical voltage was measured with an oscilloscope (DS1074Z, Rigol Technologies, Suzhou, China; sampling rate: 1 GSa/s, bandwidth: 70 MHz, horizontal div.: 5 ms, vertical div.: 200 mV) and converted to sound pressure using a sensitivity factor of 0.26 mV/Pa, as specified in the test report. Even though it is a membrane-free optical microphone, the microphone, including its mount, is inserted into the ultrasonic field, which can cause disturbances and measurement feedback.

3. Results

3.1. Ultrasound visualization: Fizeau interferometer vs. Schlieren setup

A comparison is made between the sound field visualization acquired with the Schlieren setup (cf. Section 2.3) and the Fizeau interferometer (cf. Section 2.2). The two images (in Fig. 4) both show an acoustic field generated by the same transducer array. The acquisition time of the two-dimensional images is $t_{\text{exposure}} = 37.5$ ms with a frame rate corresponding to $t_{\text{frame}} = 40$ ms. In both methods, the data is acquired in a "single acquisition mode": since the exposure time is larger than the inverse sound frequency, hardware-based averaging (of #1500) is unavoidable within one camera frame ($N = 1$). The pulse duration of the illumination was $t_{\text{on, FI}} = 200$ ns at the Fizeau interferometer and $t_{\text{on, Schlieren}} = 500$ ns (minimum possible pulse duration of the LED) at the Schlieren setup, applied in synchronized mode.

The Schlieren image (Fig. 4 a) directly displays the grayscale image of the camera without any post-processing. The spatial resolution is 431 µm. As already explained, it provides a simple and qualitative representation of the refractive index gradients $\frac{\partial n_{\text{sound}}(x,y)}{\partial x}$ caused by sound pressure modulations.

The resulting image (Fig. 4 b) from the interferometric method presents the retrieved sound pressure data as a deviation from normal air pressure with a spatial resolution of 23 µm. The raw data from the interferogram at the camera chip are processed as described in Section 2.2. The standard deviation for the interferometric sound field measurements for each pixel (x_i, y_j) exhibits a clear spatial dependence.

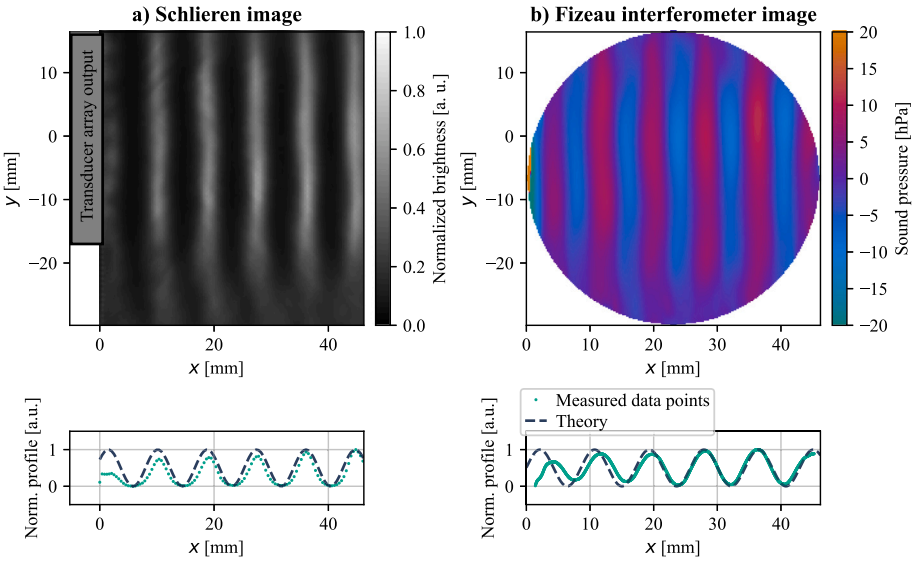

Fig. 4. Visualized measurement data of a standing ultrasonic wave, with the position of the transducer array output indicated schematically in a). The data is acquired in single acquisition ($N = 1$) with **a)** the **Schlieren setup** (lateral resolution: 431 µm) and **b)** the **Fizeau interferometer** (lateral resolution: 23 µm). The interferometric representation displays the projection of the sound pressure amplitude $p_{\text{sound}}(x, y)$ on the xy plane as a deviation from the normal air pressure in false colors, retrieved from the raw data of the optical path difference. The Schlieren image represents the sound-induced refractive index gradients. Below the images, a profile of the 2D representations at $y = 0$ mm can be seen. The normalized measurement data (green dots) is compared with an ideal theoretical cosine curve (black dashed line) according to Eq. (2). For additional information regarding the measurement uncertainty of the interferometric sound field measurement, see Appendix C.

The average standard deviation over the region of interest is ±50 Pa. Further information regarding measurement uncertainty can be found in Appendix C.

The two images in Fig. 4 show the same acoustic wavelength, despite the underlying physical phenomena responsible for enabling the visualization of sound fields being different. The ultrasonic wave has an almost planar acoustic wavefront (along y axis). The pressure distributions are approximately cosine-shaped in the x direction, as can be seen in the (green solid) profile. This indicates the negligible presence of nonlinear acoustic effects in this dataset confirming the reliability of linear approximations. The interferometric measurement data profile aligns closely with the (black dashed) theoretical curve, thus indicating the expected sound frequency of $f_{\text{sound}} = 40$ kHz.

Using Fizeau interferometry compared to the Schlieren technique has several advantages: The interferometric phase images feature better spatial resolution. The Fizeau images from this experiment demonstrate a resolution enhancement by a factor of 18 relative to the Schlieren images. However, this phenomenon is also, but not only, attributed to the use of different camera models. Furthermore, the laser beam of the Fizeau interferometer is collimated in the sample area. In comparison with the Schlieren method, the Fizeau interferometer provides additional quantitative data but requires a more complicated evaluation procedure.

3.2. Quantitative measurements: fizeau interferometer vs. xarion microphone

The Fizeau interferometer data contain the quantitative phase information necessary for retrieving the sound pressure p_{sound}. Subsequent analyses involve a comparison of these interferometric results with those obtained from an alternative measurement methodology for quantitative sound pressure data. Therefore, the sound pressure was measured with the Xarion optical microphone (cf. Section 2.4).

Fig. 5 illustrates the profile of the sound pressure amplitude p_{sound} as a function of y position. Here, the absolute values are presented. The z-position is set to the center of the transducer array ($z_{\text{center}} = 0$ mm), while the x-position is centered between the transducer array and the reflector, resulting in a distance of $x_{\text{center}} = 23.6$ mm from the sound source ($q = 11$; $x_{\text{center}} \hat{=}$ max. amplitude). The Xarion sound pressure data$|p_{\text{sound}}(x_{\text{center}}, y, z_{\text{center}})|$ shows three repeated scans over the y direction. These data fluctuate with approx. ±10 mV which corresponds to less than 1% in total. The data sets themselves vary from each other due to temporal fluctuations of the acoustic field.

To obtain the Fizeau data, the interferometric sound pressure data $|p_{\text{sound}}(x_{\text{center}}, y, \int dz \cdot z)|$ are taken, and the amplitude is extracted at the corresponding measurement position of the Xarion slices.

The comparative analysis of the data indicates a clear correlation. However, there is a physical key difference between the two measurement methods. The Fizeau interferometry provides an integrated measurement of the optical path length in the z-direction, representing an estimate of the acoustic pressure at a specific point in space. Whereas the optical microphone yields a localized, almost pointwise pressure signal. Thus, the laser can be influenced by distorting signals, leading to an impact on quantitative results. This phenomenon is particularly notable when the acoustic wavefronts are no longer perfectly planar, but not for pointwise measurements taken by the optical microphone. On the other hand, the optical microphone is inserted into the sound field. This can also cause disturbances which, in turn, can give rise to deviations in the measured quantities. Further discrepancies can be attributed to the relatively high measurement uncertainty, which is discussed in more detail in Appendix C.

The method of using the Fizeau interferometer instead of a microphone to characterize ultrasonic fields has the advantage of not causing interaction with the field itself and, more importantly, no scanning is needed. In this single acquisition mode the data over the entire image is acquired simultaneously in 37.5 ms. It can even be accelerated by adjusting the camera settings accordingly (or for higher ultrasonic frequencies by applying another method, such as frequency division multiplexing for temporal super-resolution [51]). This is, in general, a significant improvement over all scanning-based methods, such as acoustic and optical microphones or laser Doppler vibrometers. This allows averaging to eliminate random errors while keeping measurement durations low and enables applications that require the current status of the sound field. For example, when performing long-term measurements (every 30 min) to observe any drift in the sound field, or when direct feedback is needed

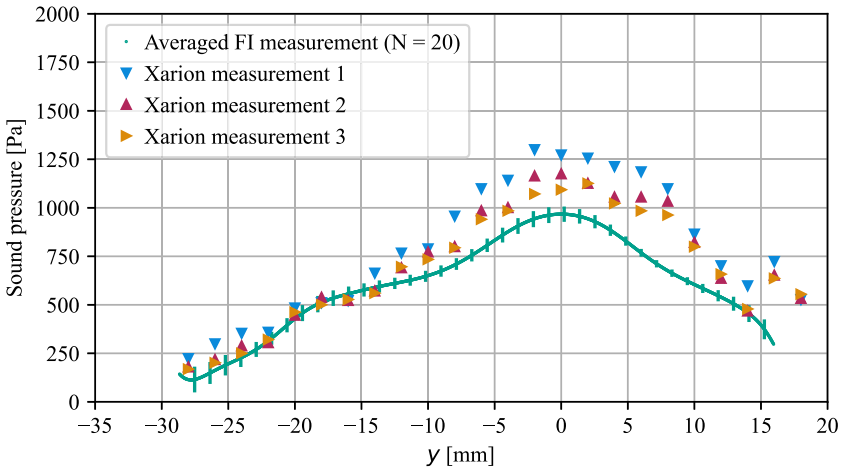

Fig. 5. The quantitative measurement of sound pressure amplitude was compared in terms of magnitude using two methods: the Fizeau interferometer (green data points) and the Xarion optical microphone (triangles: blue, red, orange). Therefore, the data were acquired over the y direction (at $x_{\text{center}} = 23.6$ mm, $z_{\text{center}} = 0$ mm). The Fizeau interferometry (FI) data were averaged over $N = 20$ measurements. The vertical error bars (green) were added only at intervals of 50 pixels (for better visibility purposes) according to the standard deviation.

while changing the emitting angle of the transducer array. With standing sound waves, especially for applications in the field of acoustic levitation, it is of great importance that the distance to the reflector is precisely adjusted. With the Fizeau interferometer, the resonance condition can be directly monitored and accordingly corrected.

Moreover, the interferometric approach provides only an approximation of the local acoustic pressure distribution. This limitation arises from the integration of refractive index modulations along the optical axis z. Thus, the extracted pressure amplitudes cannot be directly compared one-to-one with point-like microphone measurements. Consequently, the local pressure values should be regarded as estimates rather than absolute quantities. Nevertheless, by applying the model for calculating the effective sound field width (cf. Eq. (B.11) and Eq. (B.12)), the interferometric data can be related to the acoustic field with sufficient fidelity. This provides a meaningful approximation of the sound pressure distribution generated by the transducer array.

Assuming this sound field is rotationally symmetric by 90° steps ($y = z$), an alternative method for data matching can be proposed. Therefore, a numerical integration of the Xarion measurements over the y direction is performed. Subsequently, the refractive index and the optical phase shifts can be retrieved for one specific point in space. These results show good agreement $\Delta\varphi < 2\%$ (e.g., for Xarion measurement 3, cf. Fig. 5) with the phase value obtained with the Fizeau interferometer (data set shown in Fig. 4) at the corresponding spatial position ($x_{\text{center}} = 23.6$ mm, $y = 0$ mm). This analysis not only provides a consistent validation of the quantitative Fizeau measurements, but also indicates that acoustic pressure modulations outside the measurement range of the Xarion optical microphone have only a negligible impact on the resulting interferometrically measured phase shift.

In general, the Fizeau interferometer is a reliable contactless method for rapidly characterizing ultrasonic fields in 2D. The visualization and the quantitative results obtained demonstrate a satisfactory outcome. Although the Fizeau interferometer still has room for improvement, this method integrates the advantages of both alternatives into a single measurement technique.

4. Discussion and outlook

This study demonstrated that the Fizeau interferometer is a powerful contactless method for both 2D rapid visualization and quantitative characterization of ultrasonic fields. Operating the Fizeau interferometer in synchronized mode extends its use beyond the main application of surface roughness measurements and demonstrates its suitability for the characterization of ultrasonic fields. As the laser of the interferometer is pulsed with the ultrasonic frequency, this approach allows for the visualization of both standing waves (see Fig. 4) and propagating acoustic waves (without a reflector).

Table 1
Relative comparison of characterization methods for ultrasonic fields.

Criterion	Schlieren Imaging	Xarion Microphone	Fizeau Interferometer
Invasivity	non-contact	inserted optical mic.: 5 mm × 38 mm	non-contact
Measurement dimension	2D (projection)	0D (local)	2D (projection)
Acquisition time (2D)[a]	fast (40 ms)	slow (> 1 h)	fast (40 ms)
Quantification	normally no (but possible)	yes (SPL)	yes (estimated p_{sound})
Spatial resolution[a]	431 μm	2 mm	23 μm

[a] The exact value depends on the camera used and its settings. It can be improved by using a better or faster camera.

In comparison, Schlieren imaging measures the refractive index gradients $\frac{\partial n_{\text{sound}}(x,y)}{\partial x}$, while Fizeau interferometry measures the refractive index modulations $n_{\text{sound}}(x, y)$ directly. However, this advantage comes with a more complex setup and evaluation process. Compared to Xarion microphone measurements, Fizeau interferometry offers a 2D estimation of the sound pressure data within a single acquisition event of the camera, thus avoiding the need for time-consuming scanning. Table 1 provides a short overview of the three investigated methods.

The results highlight the contribution of this comparative study: Fizeau interferometry (operating in synchronized mode) combines qualitative imaging with the estimation of quantitative sound pressure values in a single acquisition event.

4.1. Limitations

The quantitative determination of sound pressure is based on the assumption that refractive index modulation $n\_\text{sound}(x, y)$ (cf. Eq. (5)) fully accounts for $p\_\text{sound}(x, y)$. While temperature effects were estimated to be negligible, future studies should examine them in greater detail.

Regarding the permitted **acoustic wavefront shape** it is imperative to acknowledge that the quantitative Fizeau data represent a two-dimensional projection integrated along the z axis. This involves

using an appropriate estimation method (I., II., or III., see Appendix B for the sound field width. This approximation becomes critical when the sound field deviates from the planar wavefronts of a basic standing or propagating wave. Other wavefront shapes and non-stationary fields, including e.g., spherical waves, amplitude modulation, or beam steering, can be visualized with this Fizeau interferometer. However, for the quantitative analysis a more complex evaluation approach is required. A potential enhancement could be achieved through the implementation of a three-dimensional reconstruction of the acoustic field. For rotationally symmetric acoustic fields, this can be performed using the Hankel Fourier algorithm [19]. In the case of non-rotationally symmetric transducer arrays, a more complex method must be considered. However, the objective may be achieved using physics-informed neural network approaches [52,53].

The supported **ultrasonic frequency range** of the Fizeau interferometer depends on the lateral resolution of the optical system. Within the scope of this study, the interferometer was designed to support sound frequencies of 40 kHz and thus to cover the lower ultrasonic region. The lower frequency limit of this proposed setup is primarily determined by the size of the investigated sample area (($\emptyset_{\text{sample}} = 50.8$ mm)). If at least one full acoustic wavelength is to be imaged, the lowest possible acoustic frequency can be estimated to be 6.8 kHz, which is within the audible range.

The upper limit of the sound frequency range is related to the minimal resolvable acoustic wavelength Λ_{min}. Thus, the spatial resolution can be estimated using the diameter of the sample area, the pixel size ($d_{\text{px}} = 3.45$ µm), and the chip size ($d_{\text{chip}} = 7.452$ mm) of the camera: $d_{\text{px}} \cdot \frac{\emptyset_{\text{sample}}}{d_{\text{chip}}}$. Additionally two factors have to be taken into account. The first factor (of 2) considers the Nyquist criteria and the second factor (of 10) is due to the spatial carrier frequency analysis. This loss in spatial resolution (for $3x3$ kernels) with respect to the temporal phase shifting technique is in order to achieve 90% signal height [42].

$$f_{\text{sound}} \leq \frac{c_{\text{sound}}}{\Lambda_{\text{min}}} = \frac{c_{\text{sound}}}{2 \cdot 10 \cdot d_{\text{px}} \cdot \frac{\emptyset_{\text{sample}}}{d_{\text{chip}}}} \tag{9}$$

Therefore, ultrasonic frequencies up to 730.7 kHz can be characterized with this Fizeau interferometer.

Furthermore, the ultrasonic transducers to be measured must provide a **sound pressure level SPL** high enough to be detectable with an interferometer. To experimentally determine the lower sound pressure limit of this interferometer, the number of active acoustic transducers in the transducer array is reduced to one. This causes the acoustic field to change from a plane wave to a spherical wave. Nevertheless, the investigation provides a meaningful indication of the interferometer's detection limit. Under the condition that the measurements are averaged (e.g., $N = 100$ acquisitions) even the sound field of a single transducer ($\text{SPL}_{\text{min}} = 120$ dB) can be visualized. Consequently, at lower sound pressure levels, the number of measurements must be increased to enhance the signal-to-noise ratio and thereby enable the measurement of these fields.

The upper sound pressure limit for obtaining quantitative pressure data is defined as the threshold beyond which acoustic nonlinearities (see Appendix A) become dominant. Nonetheless, observations indicate that the visualization technique itself extends beyond this threshold. Future experiments with resolution test targets will investigate the accessible frequency and dynamic ranges of the interferometer. A detailed analysis of the instrument transfer function, and thus the frequency-dependent impulse response $H(f)$, will be an optional additional research project and very valuable for calibration and correction processes [54,55].

Real-time imaging of the acoustic field using a Fizeau interferometer is not yet possible, even though the acquisition of the interferogram occurs within a single camera frame. The data analysis is currently performed offline. In general, the evaluation method, based on spatial carrier frequency analysis, requires only one acquisition (see Fig. 4, where $N = 1$) and therefore offers the potential for live imaging of ultrasonic fields. Optimizing the evaluation code for speed could further enable real-time characterization, as in the Fizeau interferometer *Zeiss DIRECT 100 NT* [40,46]. The pixel-level Lissajous figure and ellipse fitting [56] represent a promising approach for enhancing the evaluation in future studies. This allows for investigations of transient dynamic behavior, e.g., of acoustic levitators. Alternatively, evaluating interferometric video sequences may offer a practical approach.

Furthermore, an acousto-optic modulator is implemented to modulate the interferometer's laser source. This is attributed to the hardware-based frame rate limitations of the camera. By using a high-speed camera, the proposed approach could be implemented even without an AOM. It is imperative to note that the maximum attainable frame rate must be at least equal to the ultrasound frequency being measured.

Additionally, the application of this interferometric technique is not limited to air as the **sample medium**. An alternative future approach would be to consider these Fizeau measurements with a water container inserted into the sample area [57–60]. This could significantly expand the range of applications towards water-coupled ultrasonic measurements.

5. Conclusion

In conclusion, this paper introduces an experimental approach and comparative study for interferometric visualization and quantitative characterization of air-coupled ultrasonic fields. The results demonstrate that the Fizeau interferometer enables reliable quantification of ultrasonic waves, and future research will further establish its potential as a versatile method for characterizing ultrasonic fields.

CRediT authorship contribution statement

Regina Schuster: Writing – review & editing, Writing–original draft, Software, Methodology, Investigation, Conceptualization. **Marius Foith:** Writing – review & editing, Validation, Software, Methodology, Investigation. **Jan Helge Dörsam:** Writing – review & editing, Resources, Conceptualization. **Sören Soennecken:** Writing – review & editing, Resources. **Yannick Schrödel:** Writing – review & editing, Resources. **Christoph M. Heyl:** Writing – review & editing, Resources, Conceptualization. **Mario Kupnik:** Writing – review & editing, Resources, Conceptualization. **Anne Harth:** Writing – review & editing, Supervision, Resources, Project administration, Funding acquisition, Conceptualization.

Funding

This work was supported by the Carl-Zeiss-Stiftung Germany [Wildcard - SOPHIMA project]; the German Federal Ministry of Research, Technology and Space (BMFTR) within the "FH-Impuls" program (SmartPro, Smart-LIGHT project) [grant number 13FH4I10IA]; the Deutsche Forschungsgemeinschaft (DFG, German Research Foundation)–[grant number INST52/22-1]. The publication was funded by Aalen University of Applied Sciences.

Declaration of generative AI and AI-assisted technologies in the writing process

During the preparation of this work, the authors used ChatGPT and DeepL for translation and as assistance tools for formulation. After using these tools, the authors reviewed and edited the content as needed and take full responsibility for the content of the published article.

Declaration of competing interest

The authors declare the following financial interests/personal relationships which may be considered potential competing interests:

Regina Schuster reports that financial support was provided by Carl Zeiss Stiftung. Regina Schuster reports that financial support was provided by the German Research Foundation. Regina Schuster reports that financial support was provided by the German Federal Ministry of Research, Technology and Space. If there are other authors, they declare that they have no known competing financial interests or personal relationships that could have appeared to influence the work reported in this paper.

Appendix A. Nonlinear acoustic effects

At exceedingly high sound pressure amplitudes (on the order of SPL $\gtrsim$ 155 dB in air), nonlinear acoustic effects become significant. In this regime, the relationship between acoustic pressure and density can no longer be approximated as linear, but is governed by a nonlinear equation of state. The local propagation speed of sound depends on the density of the medium, which is modulated by the sound pressure itself. Therefore it becomes amplitude-dependent. This leads to faster propagation of compression phases compared to rarefaction phases, resulting in waveform distortion, progressive wave steepening, and the generation of higher harmonics.

The transition between linear and nonlinear acoustic regimes is gradual and depends on several parameters, including the propagation distance, sound frequency, and medium properties. According to the recommendation of the "Deutsche Gesellschaft für Akustik" (DEGA [61]), linear acoustics is a valid approximation as long as the acoustic Mach number remains small:

$$M_a = \frac{v_{particle}}{c_{sound}} \ll 1, \tag{A.10}$$

where $v_{particle}$ denotes the particle velocity. For plane waves in the linear regime, this can be related to the acoustic pressure p_{sound} and the air density ρ_{air} using $v_{particle} = \frac{p_{sound}}{(\rho_{air} \cdot c_{sound})}$. This condition is met for the investigations of this work (using $p_{sound,max} \approx 1100$ Pa, and $\rho_{air} = 1.2$ kg/m^3; $M_a = 0.008$). For larger amplitudes, this condition becomes violated, and the linear wave equation (cf. Eqs. (1) and (2)) is no longer sufficient. A more accurate description requires nonlinear wave equations such as the Westervelt equation [62].

Regarding the proposed method for characterizing ultrasonic fields, it is important to distinguish between physical limitations, qualitative visualization, and quantitative pressure evaluation. The interferometric approach itself is not inherently restricted to linear acoustic fields and can be applied to visualize high-power ultrasonic fields exhibiting nonlinear effects, such as waveform steepening. Indeed, there is a limitation regarding the avoidance of phase jumps in the phase shift retrieved from the interferogram, which are induced by nonlinear acoustics and exceed a value of π. However, in this paper, the retrieval of quantitative sound pressure data relies on linear relations between refractive index variations and acoustic pressure (cf. Eqs. (5) - (7)). In the nonlinear regime ($p_{sound} \ll p_{air}$), these relations become invalid or require appropriate nonlinear corrections, and neglecting these effects may lead to systematic errors in the estimated pressure field.

Appendix B. Methods to determine the sound field width

Fig. B.6 provides a graphical overview of the three methods discussed in Section 2.2. A comparative analysis was performed to evaluate these methods in the context of cross-validation. The results show that the deviations remain within ΔSPL $\approx$ 1 dB, which is on the same order of magnitude as the intrinsic sound pressure fluctuations. This demonstrates that, even though the selected method does have an impact on the quantitative results, the influence is constrained.

B.1. Simulation to compute the effective sound field width

The effective width of the sound field can be determined using a simulation (Method III), as outlined in the following:

Therefore, a three-dimensional simulation was developed using the propagation of the sound field $p(x, y, z)$ based on the angular spectrum approach [36] to obtain quantitative width values as described in the following. The input aperture for this simulation method corresponds to the real aperture of the transducer array, described in Section 2.1 (8×8 single ultrasonic sources). Then, the Fourier transform is used to calculate the sound pressure field along its propagation direction x. For each pixel in the xy plane, there is a pressure distribution $p(x_i, y_j, z)$ over z with a local maximum $p_{max}(x_i, y_j)$. The numerical integral:

$$I_{integral}(x_i, y_j) = \int p(x_i, y_j, z) dz \approx \sum^{Nz} p(x_i, y_j, z) \cdot \Delta z.f \tag{B.11}$$

over z, together with the maximum $p_{max}(x_i, y_j)$, is used to calculate an effective sound field width for each pixel:

$$w_{eff}(x_i, y_j) = \frac{I_{integral}(x_i, y_j)}{p_{max}(x_i, y_j)}. \tag{B.12}$$

While this is still an approximation, it improves the calculation compared to using $w_{aperture}$ of Method I by considering the location-dependent characteristics of the sound field width. In Section 2.2 w_{sound} is replaced with the effective, pixel-dependent sound field width $w_{eff}(x_i, y_j)$ from the simulation.

When using this simulation, it is important to apply a sufficiently large initial calculation domain, as inadequate dimensions result in the effective sound field widths being dependent on the calculation domain. However, this simulation has several advantages and is a suitable approach, if the sound field width changes in the x direction, e.g., for spherical waves. Furthermore, it can represent width values for sound fields that are not rotationally symmetric by 90° steps. This method should also be selected in cases where spatially extended sound fields cannot be fully projected onto the sample area. Due to the integral nature of interferometric laser measurement, this method, which is based on numerical integrals, is appropriate for evaluating the experimentally determined width values.

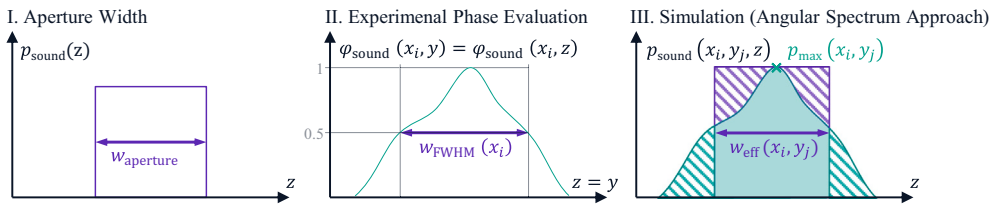

Fig. B.6. These graphs illustrate three different methods for determining the sound field width. Method I defines the sound field width as a constant and equal to the aperture output of the transducer array ($w_{aperture}$). Method II uses an experimental approach in which the sound field width is defined as the full width at half maximum (FWHM) of the interferometrically acquired phase data ($w_{FWHM}(x_i)$). If the sample area is large enough, this value can be determined depending on the x direction. In Method III the sound field width is obtained using a simulation based on the angular spectrum approach ($w_{eff}(x_i, y_j)$). This is further explained in Appendix B.1.

Appendix C. Measurement uncertainty according to GUM

The measurement uncertainty of the Fizeau interferometry data was evaluated following the guidelines of the Guide to the Expression of Uncertainty in Measurement (GUM) [63]. In this context, the measurand is the sound pressure amplitude $p_{\text{sound}}(x, y)$. The corresponding measurement equation is obtained by substituting Eq. (8) into Eq. (6). The quantities refractive index of air n_{air}, ambient pressure p_{air}, laser wavelength λ_{laser}, and effective sound field width $w_{\text{eff}}(x_i, y_j)$ were considered as Type B input variables. The phase shift $\varphi(x, y)$, on the other hand, was treated as a Type A contribution, with its uncertainty estimated from the standard deviation of the mean of repeated measurements ($N = 20$). These standard deviations are shown as error bars (at intervals of 50 pixels for better visibility purposes) in Fig. 5 and also serve as indicators of measurement repeatability. It should be noted that variations in the ultrasonic field itself are also reflected in the phase shift statistics. These could be due to slow temperature drifts caused by the heating of the transducer array during continuous operation.

The resulting GUM analysis yields an expanded uncertainty (coverage factor $k = 2$) of ± 40 Pa for the reconstructed sound pressure amplitude. A sensitivity analysis reveals that the effective sound field width $w_{\text{eff}}(x_i, y_j)$ contributes the largest share to the uncertainty ($\sim 75\%$), followed by the phase shift $\varphi(x, y)$ ($\sim 23\%$). The remaining quantities (n_{air}, p_{air}, λ_{laser}) have only a marginal influence of less than 1% each.

For the Xarion microphone measurements, the GUM evaluation results in an expanded uncertainty (coverage factor $k = 2$) of ± 80 Pa. Here, the main contribution is the oscilloscope voltage measurement, which is treated as a Type A quantity. Despite the limited number of measurements for the Xarion data per y position ($N = 3$), the fluctuations of the acoustic field are included in the estimated measurement uncertainty.

Data availability

Data will be made available on request.

References

[1] D.E. Chimenti, Review of air-coupled ultrasonic materials characterization, Ultrasonics 54 (7) (2014) 1804–1816, https://doi.org/10.1016/j.ultras.2014.02.006

[2] S.M. Mohtashamipoor, M. Reinhold, T. Herzog, Investigation of weld seams of ffp2 medical mask by air-coupled ultrasound, Research and Review Journal of Nondestructive Testing 2 (1) (2024), https://doi.org/10.58286/30166

[3] D. Foresti, M. Nabavi, M. Klingauf, A. Ferrari, D. Poulikakos, Acoustophoretic contactless transport and handling of matter in air, Proc. Natl. Acad. Sci. U. S. A. 110 (31) (2013) 12549–12554, https://doi.org/10.1073/pnas.1301860110

[4] V. Contreras, A. Marzo, Adjusting single-axis acoustic levitators in real time using rainbow schlieren deflectometry, The Review of scientific instruments 92 (1) (2021) 015107, https://doi.org/10.1063/5.0013347

[5] H.M. Reynoso-de la Cruz, E.D. Hernández-Campos, E. Ortiz-Ricardo, A. Martínez-Borquez, I. Rosas-Román, V. Contreras, G. Ramos-Ortiz, B. Mendoza-Santoyo, C.I. Zurita-Lopez, R. Castro-Beltrán, Acoustically levitated whispering-gallery mode microlasers, Opt. Laser Technol. 171 (2024) 110352.

[6] T. Takeda, T. Mabuchi, N. Takesue, N. Kubota, H. Liu, A wave detection method for air-coupled ultrasound system on human abdominal region, IEEE (2016) 004240–004244, https://doi.org/10.1109/SMC.2016.7844898.

[7] Y. Schrödel, C. Hartmann, J. Zheng, T. Lang, M. Steudel, M. Rutsch, S.H. Salman, M. Kellert, M. Pergament, T. Hahn-Jose, S. Suppelt, J.H. Dörsam, A. Harth, W.P. Leemans, F.X. Kärtner, I. Hartl, M. Kupnik, C.M. Heyl, Acousto-optic modulation of gigawatt-scale laser pulses in ambient air, Nat. Photonics 18 (2024) 54–59, https://doi.org/10.1038/s41566-023-01304-y

[8] S. Kumar, H. Furuhashi, Long-range measurement system using ultrasonic range sensor with high-power transmitter array in air, Ultrasonics 74 (2017) 186–195.

[9] A. Torkkeli, O. Rusanen, J. Saarilahti, H. Seppä, H. Sipola, J. Hietanen, Capacitive microphone with low-stress polysilicon membrane and high-stress polysilicon backplate, Sens. Actuators a Phys. 85 (1–3) (2000) 116–123.

[10] F. Attivissimo, F. Adamo, L. De Palma, A. Di Nisio, M.A. Ragolia, A.M.L. Lanzolla, Analysis of model parameters and experimental setup for accurate characterization of ultrasound phased arrays using a low-cost sensor, IEEE Trans. Instrum. Meas. 74 (2025) 1–9, https://doi.org/10.1109/TIM.2024.3522629.

[11] L. Svilainis, A. Chaziachmetovas, V. Eidukynas, T.G. Álvarez-Arenas, S. Dixon, Miniature ferroelectret microphone design and performance evaluation using laser excitation, IEEE Trans. Ultrason. Ferroelectr. Freq. Control 69 (12) (2022) 3392–3401.

[12] STMicroelectronics, IMP23ABSU datasheet, (accessed 2020, https://www.st.com/en/mems-and-sensors/imp23absu.html (17 November 2025).

[13] Hottinger Brüel & KjA/S, Brüel & KJTransducers, Product Data BP 2030 – 13 (accessed 17 November 2025) 2021, https://www.bksv.com/media/doc/bp2030.pdf.

[14] S. Zehnter, M.A.B. Andrade, C. Ament, Acoustic levitation of a Mie sphere using a 2D transducer array, J. Appl. Phys. 129 (13) (2021).

[15] S. Soennecken, S. Wismath, J.H. Dörsam, A. Herzog, C. Haugwitz, N. Demuth, H. Malang, C.M. Heyl, M. Kupnik, Resonance tuning of circular ultrasonic arrays using air-coupled waveguides, in: 2025 IEEE International Ultrasonics Symposium (IUS), IEEE, 2025, pp. 1–4.

[16] Y. Cao, G. Li, Z. Li, J. Chen, Y. Zheng, D. Zhao, Y. Yang, C. Xue, Extreme dual-parameter measurement of high static pressure and high acoustic pressure based on fibre-optic fabry-pérot sensor at 500° c, Opt. Laser Technol. 188 (2025) 112955.

[17] B. Fischer, Optical microphone hears ultrasound, Nat. Photonics 10 (6) (2017) 356–358, https://doi.org/10.1038/nphoton.2016.95

[18] L. Zipser, L. Zipser, L. Zipser, L. Zipser, L. Zipser, Reconstructing two-dimensional acoustic object fields by use of digital phase conjugation of scanning laser vibrometry recordings, Appl. Opt. 42 (29) (2003).

[19] H. Dong, Z. Yu, K.T.V. Grattan, T. Sun, T. Li, Acoustic standing wave field measurement using a laser Doppler vibrometer based on the hankel Fourier algorithm, IEEE Access 7 (2019) 139013–139020.

[20] M. Leutenegger, E. Martin-Williams, P. Harbi, T. Thacher, W. Raffoul, M. André, A. Lopez, P. Lasser, T. Lasser, Real-time full field laser Doppler imaging, Biomed. Opt. Express 2 (6) (2011) 1470–1477.

[21] A. Crockett, W. Rueckner, Visualizing sound waves with schlieren optics, Am. J. Phys. 86 (2018) 786–870, https://doi.org/10.1119/1.5042245

[22] R. Onishi, T. Kamigaki, S. Suzuki, T. Morisaki, M. Fujiwara, Y. Makino, H. Shinoda, Two-dimensional measurement of airborne ultrasound field using thermal images, Phys. Rev. Appl. 18 (2022) 1–6, https://doi.org/10.1103/PhysRevApplied.18.044047

[23] M. Schneckenburger, S. Höfler, L. Garcia, R. Almeida, R. Börret, Material removal predictions in the robot glass polishing process using machine learning, SN Appl. Sci. 4, 33 (2022), https://doi.org/10.1007/s42452-021-04916-7

[24] M. Rutsch, A. Unger, G. Allevato, J. Hinrichs, A. Jäger, T. Kaindl, M. Kupnik, Waveguide for air-coupled ultrasonic phased-arrays with propagation time compensation and plug-in assembly, The Journal of the Acoustical Society of America 150 (5) (2021) 3228–3237.

[25] A. Jäger, D. Großkurth, M. Rutsch, A. Unger, R. Golinske, H. Wang, S. Dixon, K. Hofmann, M. Kupnik, Air-coupled 40-khz ultrasonic 2D-phased array based on a 3D-printed waveguide structure, 2017 IEEE International Ultrasonics Symposium 2017 (2017) 1–4, https://doi.org/10.1109/ULTSYM.2017.8091892

[26] M. Möser, Technische Akustik, Springer Vieweg, 2015, Ch. 1, 2.2, pp. 6, 37, 40. https://doi.org/10.1007/978-3-662-47704-5

[27] J.H. Dörsam, S. Suppelt, A. Altmann, J. Liu, C. Xu, C. Haugwitz, T. Maric, D. Bothe, M. Kupnik, Robust transducer–reflector distance control in acoustic levitation, IEEE Open Journal of Ultrasonics, Ferroelectrics, and Frequency Control (2026), https://doi.org/10.1109/OJUFFC.2026.3679991

[28] M.A.B. Andrade, S. Polychronopoulos, G. Memoli, A. Marzo, Experimental investigation of the particle oscillation instability in a single-axis acoustic levitator, AIP Adv. 9 (3) (2019).

[29] W.J. Xie, B. Wei, Dependence of acoustic levitation capabilities on geometric parameters, Phys. Rev. E 66 (2) (2002) 026605.

[30] S.L. Vieira, M.A.B. Andrade, Translational and rotational resonance frequencies of a disk in a single-axis acoustic levitator, J. Appl. Phys. 127 (22) (2020).

[31] K. Bertling, J. Perchoux, T. Taimre, R. Malkin, D. Robert, A.D. Rakić, T. Bosch, Imaging of acoustic fields using optical feedback interferometry, Opt. Express 22 (24) (2014) 30346–30356.

[32] C. Wang, C. Wang, Y. Shang, X. Liu, G. Peng, Distributed acoustic mapping based on interferometry of phase optical time-domain reflectometry, Opt. Commun. 346 (2015) 172–177.

[33] Z. Šlegrová, R. Bálek, A comparison measurement of nonlinear ultrasonic waves in tubes by a microphone and by an optical interferometric probe, Ultrasonics 43 (5) (2005) 315–319.

[34] X. Zhu, A. Sun, Y. Pan, H. Zhuang, W. Liu, J. Cao, G. Zhang, Y. Yang, Z. Liang, Y. Shi, et al., An acoustic sensor based on balloon-shaped microfiber Mach-zehnder interferometer, Opt. Laser Technol. 164 (2023) 109447.

[35] K. Nakamura, Sound field measurement through the acousto-optic effect of air by using laser Doppler velocimeter, in: Conference on Lasers and Electro-Optics/Pacific Rim, Optica Publishing Group, 2001, p. MG1_5.

[36] X. Zeng, R.J. McGough, Evaluation of the angular spectrum approach for simulations of near-field pressures, The Journal of the Acoustical Society of America 123 (1) (2008) 68–76.

[37] J.A. Stone, J.H. Zimmerman, Engineering metrology toolbox: refractive index of air calculator, (accessed, 2019,. https://emtoolbox.nist.gov/Wavelength/Documentation.asp (3 September 2025).

[38] B. Edlén, The refractive index of air, Metrologia 2 (2) (1966) 71–80, https://doi.org/10.1088/0026-1394/2/2/002

[39] B.E.A. Saleh, M.C. Teich, Fundamentals of photonics, in: Wiley Series in Pure and Applied Optics, Wiley, 2007, Ch. 19. Acousto-Optics, pp. 804–833.

[40] M.F. Kuechel, The new zeiss interferometer, in: Proc. SPIE Optical Testing and Metrology III: Recent Advances in Industrial Optical Inspection, vol. 1332, 1990, pp. 655–663.

[41] K. Ishikawa, K. Yatabe, N. Chitanont, Y. Ikeda, Y. Oikawa, T. Onuma, H. Niwa, M. Yoshii, High-speed imaging of sound using parallel phase-shifting interferometry, Opt. Express 24 (12) (2016) 12922–12932.

[42] B. Dörband, H. Müller, H. Gross, Handbook of Optical Systems - Volume 5: Metrology of Optical Components and Systems, WILEY-VCH Verlag GmbH & Co. KGaA, 2012, Ch. 46.3, 46.4, 46.5, pp. 49, 54, 86, 107, 112.
[43] W. Zhu, L. Chen, Y. Yang, R. Zhang, D. Zheng, Z. Han, J. Li, Advanced simultaneous phase-shifting fizeau interferometer, Opt. Laser Technol. 111 (2019) 134–139.
[44] P.A. Khorin, A.P. Dzyuba, S.N. Khonina, Optical wavefront aberration: detection, recognition, and compensation techniques–a comprehensive review, Opt. Laser Technol. 191 (2025) 113342.
[45] E.H. Por, S.Y. Haffert, V.M. Radhakrishnan, D.S. Doelman, M. van Kooten, S.P. Bos, High contrast imaging for Python (HCIPy): an open-source adaptive optics and coronagraph simulator, in: L.M. Close, L. Schreiber, D. Schmidt (Eds.), Adaptive Optics Systems VI„ vol. 10703, International Society for Optics and Photonics, SPIE, 2018, p. 1070342, (accessed https://doi.org/10.1117/12.2314407, https://docs.hcipy.org/0.5.1/api/hcipy.mode_basis.zernike.html (8 July 2025).
[46] R. Schuster, J.H. Dörsam, S. Soennecken, Y. Schrödel, C.M. Heyl, M. Kupnik, A. Harth, Optical measurement system for the characterization of propagating and standing ultrasound waves, in: C.C. Wilcox, K. Creath (Eds.), Applied Optical Metrology VI, vol. 13603, International Society for Optics and Photonics, SPIE, 2025, p. 136030B. https://doi.org/10.1117/12.3063569
[47] S.I. Veith, G. Friege, Making sound visible—a simple schlieren imaging setup for schools, Physics Education 56 (2) (2021) 025024.
[48] R. Mariani, B. Zang, H.D. Lim, U.S. Vevek, T.H. New, Y.D. Cui, A comparative study on the use of calibrated and rainbow schlieren techniques in axisymmetric supersonic jets, Flow Meas. Instrum. 66 (2019) 218–228, https://doi.org/10.1016/j.flowmeasinst.2019.01.007
[49] F.S.L. Wörtche, F. Maucher, M. Mooiweer, G.J. Verbiest, P.G. Steeneken, Characterizing ultrasonic standing wave fields by schlieren imaging, Ultrasonics 156 (10774) (2025) 3.
[50] XARION Laser Acoustics GmbH, Datasheet eta100 ultra, (accessed (02.02.2017). https://xarion.com/ploxmedia/_1_/6c7af62aae2edcb84fff1123466236b2/Eta100+Ultra+Datasheet.pdf (29 September 2025).
[51] Y. Sun, Z. Zhong, Y. Xu, D. Song, L. Yu, L. Liu, B. Liu, M. Shan, Frequency division multiplexing for temporal super-resolution in off-axis holographic sound field imaging measurement, Opt. Laser Technol. 192 (2025) 113795.
[52] R. Ito, K. Ishikawa, R. Tanigawa, Y. Oikawa, Three-dimensional sound field reconstruction from optical projections using physics-informed neural networks, JASA Express Lett. 5 (6) (2025).
[53] R. Tanigawa, K. Ishikawa, N. Harada, Y. Oikawa, Data-driven volumetric reconstruction for optically measured sound field using physics-constrained 3D Gaussian splatting, The Journal of the Acoustical Society of America 158 (3) (2025) 2163–2175.
[54] D.M. Sykora, P. de Groot, Instantaneous measurement fizeau interferometer with high spatial resolution, in: Optical Manufacturing and Testing IX, vol. 8126, SPIE, 2011, pp. 288–297.
[55] P.J. de Groot, X.C. De Lega, K. Munechika, I. Lacey, S. Rochester, N.D. Smith, P.Z. Takacs, K. Yamada, V.V. Yashchuk, Comparison of theory with the experimental characterizaion of the spatial frequency response of interferometers using a binary pseudo-random array sample, in: Applied Optical Metrology VI, vol. 13603, SPIE, 2025, pp. 26–33, https://doi.org/10.1117/12.3065712
[56] F. Liu, Y. Wu, F. Wu, N. König, R. Schmitt, Y. Wan, Y. Xu, Precise phase demodulation of single carrier-frequency interferogram by pixel-level lissajous figure and ellipse fitting, Sci. Rep. 8 (1) (2018) 148.
[57] Q. Zhang, L. Zhang, Z. Yu, D. Xia, Cross-medium detection of underwater acoustic waves using sinusoidal phase modulated differential self-mixing interferometry, Opt. Laser Technol. 195 (2026) 114507.
[58] Y. Wang, M. Sun, Y. Cao, J. Zhu, Application of optical interferometry in focused acoustic field measurement, J. Sound Vib. 426 (2018) 234–243.
[59] L. He, F. Zhu, Y. Chen, K. Duan, X. Lin, Y. Pan, J. Tao, Ultrasonic power measurement system based on acousto-optic interaction, Rev. Sci. Instrum. 87 (5) (2016).
[60] T. Ezure, K. Mizutani, H. Masuyama, Optical measurement of sound fields estimated from multiple interference images using Mach-zehnder interferometer, Electronics and Communications in Japan (Part II: Electronics) 87 (11) (2004) 20–27.
[61] Deutsche Gesellschaft für Akustik (DEGA), DEGA-Empfehlung 101 – Akustische Wellen Und Felder, Recommendation DEGA-Empfehlung 101, DEGA, 2006. https://www.dega-akustik.de/fileadmin/dega-akustik.de/publikationen/DEGA_Empfehlung_101.pdf.
[62] M.F. Hamilton, D.T. Blackstock, et al., Nonlinear Acoustics, vol. 237, Springer, 1998, Ch. 1 - 4, pp. 7, 23–39, 52–57.
[63] Joint Committee for Guides in Metrology, Evaluation of measurement data – guide to the expression of uncertainty in measurement (gum), JCGM 100:2008 100 (2008) 1–16 (accessed 3 Sep 2025). https://www.bipm.org/documents/20126/2071204/JCGM_100_2008_E.pdf (3 September 2025).